

# Sampling and Reconstructing Angular Domains with Uniform Arrays

Silvio Mandelli, Marcus Henninger and Jinfeng Du, *Member, IEEE*

**Abstract**—The surge of massive antenna arrays in wireless networks calls for the adoption of analog/hybrid array solutions, where multiple antenna elements are driven by a common radio front end to form a beam along a specific angle in order to maximize the beamforming gain. Many heuristics have been proposed to sample the angular domain by trading off between sampling step size and overhead, where arbitrarily small angular step size is only attainable with infinite sampling overhead. We show that, for uniform linear and rectangular arrays, lossless reconstruction of the array’s angular responses at arbitrary angular precision is possible using a finite number of samples without resorting to assumptions of angular sparsity. The proposed method, sampling and reconstructing angular domain (SARA), defines how many and which angles to be sampled and the corresponding reconstruction. This general solution to scan the angular domain can therefore be applied not only to beam acquisition and channel estimation, but also to radio imaging techniques, making it a candidate for future integrated sensing and communications (ISAC). Extensive simulation results for target detection and radio imaging have demonstrated clear advantages of SARA over other considered baselines, both in terms of angular reconstruction performance and computational complexity.

**Index Terms**—Angular sampling, Angular interpolation, Analog/Hybrid beamforming, Radar imaging

## I. INTRODUCTION

The next generation of wireless networks will enable technological advancements such as human-less factories [1], [2] and integrated sensing and communications (ISAC) where radio frequency imaging of passive objects [1] could be performed on top of the legacy communications operations. The large antenna arrays deployed for massive multiple input multiple output (MIMO) communications can be leveraged for fine angular resolution to separate nearby targets as well as high beamforming gains to compensate the two-way backscatter propagation loss [3]. Since cost and power consumption of such massive arrays and their associated transceiver chains may become prohibitive, analog beamforming [4], [5] and hybrid beamforming [6], [7] have been proposed to drive multiple antenna elements by each radio front end via a network of analog phase shifters.

Silvio Mandelli and Marcus Henninger are with Nokia Bell Laboratories, 70469 Stuttgart, Germany, (e-mail: silvio.mandelli@nokia-bell-labs.com, marcus.henninger@nokia.com).

Jinfeng Du is with Nokia Bell Laboratories, Murray Hill, NJ 07974, USA, (e-mail: jinfeng.du@nokia-bell-labs.com).

This work has been submitted to the IEEE for possible publication. Copyright may be transferred without notice, after which this version may no longer be accessible.

## A. Motivation

Several beam training algorithms were proposed in the literature to design the beamforming coefficients to focus transmission or reception on an arbitrary incident angle to the antenna array [4]–[14]. Accordingly, a specific set of beamforming coefficients corresponds to sampling the angular domain of that array in a specific point. Many heuristic approaches have been proposed to determine the minimum number and which angles must be scanned in order to probe the full angular domain with desired accuracy for channel estimation or angular estimation purposes. For example, the concept of discrete Fourier transform (DFT) beamspace has been introduced in [15] to represent the angular capabilities of a uniform linear array (ULA) and uniform rectangular array (URA), proposing a solution for the set of angles that must be sampled. This concept has been extended to analog/hybrid arrays recently for channel estimation purposes [11]–[13]. In particular, the algorithm proposed in [11] and [12] performs channel estimation in the DFT domain, but requires additional overhead due to estimating two-dimensional (2D) transmit-receive angular pairs instead of a single angle, corresponding to the scenario of sensing acquisitions with an antenna array. Finally, the prior analysis makes the common assumption of antenna arrays with half wavelength spacing, that does not allow generalization of their conclusions to either a generic ULA or URA.

Differently from previous works on beamforming at millimeter wave (mm-Wave) at higher frequencies, passive sensing applications in 6th generation (6G) networks require the full image of the sensed environment rather than a sparse angular representation, that is typically assumed [7]. This raises the challenge of interpolating the available angular acquisitions, determining the angular representation of the channel/environment at every possible angle, as if infinite angular acquisitions were possible. The interpolation and reconstruction literature [16] has largely ignored the non-linearity of the generated phase shifts of ULAs and URAs at each antenna element with respect to the incident angle. For example, among the few which consider angular domains, the interpolation based on the effective aperture distribution function (EADF) [17] proposes uniform sampling in the angular domain over the angular intervals of interest. However, in this work we show that this leads to distortion in the angular response reconstruction. More recent work accounts for this non-linearity for hybrid uniform cylindrical arrays (UCyAs) in [18], where the authors proposed an efficient tensor-based angular estimation algorithm exploiting sparse

array theory, achieving better resolution and lowering the number of required radio front ends. Similarly, in [14], the authors considered linear angular interpolation for hybrid UCyA angular array responses. However, both [14] and [18] focus on UCyA, making the angular domain representation, its sampling, and its reconstruction very different from ULA and URA. In particular, the proposed linear interpolation cannot achieve lossless angular domain reconstruction, which is provided by the formulae derived in this work. Recent work on radio imaging with arrays [10] performs acquisitions with fine sampling of the angular domain, generating many (redundant) acquisitions with large overhead and reducing the amount of radio resources available for ISAC. Moreover, these long acquisitions in dynamic scenarios would cause a signal change during the acquisitions, distorting the desired image, as will be discussed later.

Summarizing the problem, with the surge of analog and hybrid arrays in wireless communications, determining which angles to be sampled is critical to reduce acquisition time without losing the channel and environment information that can be gathered by the antenna array. Then, proper interpolation of the available angular samples is pivotal for imaging applications in future wireless networks.

### B. Our contributions

In this work we leverage the Fourier duality between the space where ULA antennas are placed and the normalized angular frequency (NAF), defined as the sine of the incident angle with a linear coefficient depending on the antenna spacing and wavelength. This allows us to

- derive the sampling and reconstructing angular domain (SARA) criterion for ULA and URA angular response acquisitions, determining how many and which angles must be sampled such that lossless reconstruction can be done for any possible angle without resorting to the channel sparsity assumption. SARA is built by applying the Nyquist-Shannon sampling theorem [19] to the array space and the NAF domains. Then, the Whittaker-Shannon interpolation has been used as starting point to derive the formulas to reconstruct the angular response. The final solution is shown to coincide with the trigonometric interpolation [20] of the angular samples, if they are taken uniformly in the NAF domain;
- prove that a computationally efficient implementation of the lossless reconstruction can be obtained as a particular case of DFT interpolation [21];
- compare via extensive numerical simulations the performance of SARA in both angular estimation and RF imaging against interpolation baselines and the multiple signal classification (MUSIC) algorithm [22], showing SARA approaches the root Cramér-Rao lower bound approximation (RCA) for NAF estimation of an impulsive target [23].

The proposed SARA is particularly useful with imaging techniques, where one is not interested in a sparse representation of the channel, but rather in its overall response at every angle visible by the antenna array, like in [9], [10]. However, we

show in our numerical evaluations that the proposed non-sparse reconstruction is valid also to estimate the sparse angular components of wireless channels, that is the typical assumption for mm-Wave and higher carrier frequency systems [7].

### C. Paper organization

The rest of the paper is organized as follows. Models and preliminaries are given in Section II. The SARA angular sampling and reconstruction over a generic ULA is formalized in Section III. Section IV elaborates on a few practical applications of SARA: ULA only at transmitter/receiver, ULA at both ends, and generalization to URA scenarios. Section V presents numerical experiments of single and multiple target angular estimation in a mono-static sensing scenario with full-duplex ULA scans in the azimuth domain, as well as a 2D imaging example to visualize each step of SARA.

**Notation:** row vectors are in bold lowercase and scalars are unbolded. The  $n$ -th element of a vector  $\mathbf{v}$  is denoted as  $\mathbf{v}_n$ . A row vector of  $N$  zero (or unitary) elements is denoted as  $\mathbf{0}_N$  (or  $\mathbf{1}_N$ ). We define  $\mathbf{I}_N$  as an identity matrix of  $N \times N$  elements. The element-wise (Hadamard) product of two vectors is denoted by  $\odot$ . Sets are denoted in mathematical italic capital letters (e.g.,  $\mathcal{L}, \mathcal{D}$ ), while  $\mathbb{Z}, \mathbb{N}_0$  are reserved for sets of integers, and natural numbers with zero, respectively. The rectangle function  $\text{rect}(x)$  equals 1 for  $x \in [-0.5, 0.5]$  and zero elsewhere.  $\delta(x)$  is the Dirac delta function. The modulo function is defined as  $\text{mod}_n(x) = x - n\lfloor x/n \rfloor$ .

## II. MODELS AND PRELIMINARIES FOR ARRAY AND ANGULAR DOMAINS

### A. Antenna array model

We assume to sense the environment over a single angular dimension - the azimuth - with a ULA by transmitting or receiving focused beams of narrowband signals with wavelength  $\lambda$ . Let  $N$  be the number of array elements that are equally spaced  $d$  apart, whose absolute positions are defined by the set

$$\mathcal{X} = \{x_0, \dots, x_{N-1}\}, \text{ with} \\ x_n = \left(-\frac{N-1}{2} + n\right)d, \quad n = 0, \dots, N-1. \quad (1)$$

We then define the NAF as  $\ell = \frac{d \sin \theta}{\lambda}$ , and the array aperture line (AAL)  $x'$  as a virtual position axis with unitary antenna spacing, i.e.,  $x' = x/d$  and  $x'_n = x_n/d$ . See Fig. 1 for an illustrative example with  $N = 8$ .

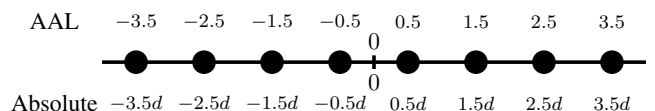


Fig. 1: ULA example with  $N = 8$  elements, with their absolute location  $x$  and AAL  $x' = x/d$ .

The signal at the  $n$ -th element of such an array with a unitary amplitude planar wave at incident angle  $\theta$  can be seen as the sampled response in the AAL domain

$$a_n(\ell) = e^{j2\pi x'_n \ell}. \quad (2)$$

**Remark 1.** The NAF axis has a physical representation in the interval  $[-d/\lambda, d/\lambda]$  of extension  $2d/\lambda$ , corresponding to incident angles in  $[-\pi/2, \pi/2]$ . However, the NAF can assume any real value in  $(-\infty, +\infty)$  due to the periodic array response (see Sec. II-B).

From Eq. (2), given an arbitrary incident integral of planar waves, describing the sparse angular response (or image) of the scenario, one can write the signal at the  $n$ -th antenna as

$$a_n = \int_{-\frac{d}{\lambda}}^{\frac{d}{\lambda}} L(\ell) e^{j2\pi x'_n \ell} d\ell, \quad (3)$$

where  $L(\ell)$  is the coefficient of the incident planar wave with NAF  $\eta$ . Eq. (3) establishes a Fourier duality between the NAF  $\ell$  and the AAL  $x'$ . This means that one domain can be obtained as the (inverse) Fourier transform of the other. Increasing element spacing  $d$  has benefits of antenna diversity and angular resolution, due to larger array aperture [24], but at the cost of increased possibility of aliases in the angular domain. This can be explained by the fact that antenna elements in a ULA uniformly sample the signal in the AAL domain at the antenna locations, creating replica every unitary shifts in its Fourier transform [25], i.e., the NAF domain.

Leveraging the sampling theorem [19], if one wants to avoid aliases in the NAF over the interval  $[-d/\lambda, d/\lambda]$ , one has to sample the AAL axes by keeping a gap between the ULA's antennas, satisfying the following (well-known) condition

$$\underbrace{1}_{\text{AAL Sampling frequency}} \geq \underbrace{\frac{2d}{\lambda}}_{\text{NAF extension}} \Leftrightarrow d \leq \frac{\lambda}{2}. \quad (4)$$

Note that if the NAF aperture of interest is reduced to  $2dp/\lambda$ , with  $p < 1$ , the AAL domain could be sampled more coarsely, i.e.  $d \leq \lambda/(2p) \geq \lambda/2$ . In the special case of  $d = \lambda/2$ , NAF replica are generated at unitary period. Therefore, one could only consider  $[-\pi/2, \pi/2)$  or  $(-\pi/2, \pi/2]$  as angular intervals without aliasing.

### B. Impact of array aperture

For a ULA with  $N$  antenna elements, the array total aperture in the AAL domain induces a low pass frequency effect in the NAF domain, due to the Fourier duality discussed earlier. To maximize the ULA's response on a given NAF  $\ell$ , the array matched beamformer can be applied to get the array's NAF response

$$L_N(\ell) = \frac{1}{N} \sum_{n=0}^{N-1} a_n e^{-j2\pi x'_n \ell}, \quad (5)$$

where  $a_n$  is again the signal at the  $n$ -th antenna element. For analog beamforming, the array focuses on a different NAF  $\ell$  (thus sampling along a corresponding direction in the angular domain) by applying weights  $w_n(\ell) = e^{-j2\pi x'_n \ell}$  as in (5).

From Remark 1, one can notice that  $L'_N(\ell)$ ,  $\ell \notin [-d/\lambda, d/\lambda]$  focuses on a NAF that does not represent a true physical angle.

**Lemma 1.** The ULA NAF response (5) of a single incident planar wave at NAF  $\eta$  is

$$L_N(\ell, \eta) = \frac{\sin(\pi N(\ell - \eta))}{N \sin(\pi(\ell - \eta))} = D_N(\ell - \eta). \quad (6)$$

*Proof.* See Appendix A.  $D_N(\ell) \equiv \sin(\pi N\ell)/(N \sin(\pi\ell))$  is the Dirichlet kernel of order  $N$ .  $\square$

The main lobe half-width and period of the Dirichlet kernel in (6) correspond to the multi-target resolution of  $1/N$  and unitary aliasing, respectively, of NAF estimation algorithms.

**Remark 2.** Amplitude scaling coefficients could be applied at each antenna element to suppress side-lobes at the price of beam gain. In particular, (5) can work with any arbitrary, hence optionally scaled, complex signal at each antenna element.

We define now an auxiliary NAF response

$$L'_N(\ell) = L_N(\ell) e^{-j2\pi \frac{N-1}{2} \ell}, \quad (7)$$

where we leveraged the Fourier duality to translate the AAL axes such that the first antenna element is at AAL equal to zero. This allows to write the following Lemma.

**Lemma 2.** The auxiliary NAF response of a ULA defined in (5) is a periodic function given by

$$L'_N(\ell - k) = L'_N(\ell), \text{ with } k \in \mathbb{Z}. \quad (8)$$

*Proof.* The complete proof is in Appendix B.  $\square$

**Remark 3.** The array extension in AAL is in  $[-\frac{N-1}{2}, \frac{N-1}{2}]$ . After the auxiliary translation in AAL, the extension is shifted to  $[0, N - 1]$ .

## III. ANGULAR SAMPLING AND RECONSTRUCTION

In this section, we propose a method to sample and reconstruct the angular domain (SARA) using analog ULA systems. With SARA, the reconstruction is “loss-less” in the sense that it allows the perfect angular response reconstruction as if noise-less infinite scans at every angle were performed using the considered ULA. The Nyquist-Shannon sampling theorem [19] states that a sufficient condition to completely determine and reconstruct a generic time signal with (positive and negative) bandwidth  $B$  is to sample it uniformly at points  $1/B$  apart. Then, the original signal can be perfectly reconstructed into  $x_r(t)$  from its infinite samples  $x(nB^{-1})$  by low pass filtering them, getting the well known Whittaker-Shannon interpolation formula

$$x_r(t) = \sum_{n=-\infty}^{+\infty} x(nB^{-1}) \text{sinc}\left(B\left(t - \frac{n}{B}\right)\right), \quad (9)$$

where  $\text{sinc}(x) = \sin(\pi x)/(\pi x)$ . We frame the problem of sampling and reconstructing a ULA angular response by working in the AAL and NAF domains, leveraging their Fourier duality. One can notice from (1) that the AAL domain can

avoid aliasing and have equally spaced samples if the replica generated from sampling are  $N$  apart from each other. Therefore, we can sample the ULA's NAF response with frequency  $N$ , obtaining  $L(nN^{-1})$ . Applying (9), the reconstructed NAF response ( $B = N^{-1}$ ) is obtained as

$$R_N(\ell) = \sum_{n=-\infty}^{+\infty} L_N\left(\frac{n}{N}\right) \text{sinc}\left(N\left(\ell - \frac{n}{N}\right)\right). \quad (10)$$

Here, we make the auxiliary NAF response derivation explicit, since the periodic behavior of the NAF response  $L_N(\ell)$  is not trivial as seen in Lemma 2.

$$R'_N(\ell) = \sum_{n=-\infty}^{+\infty} \left( L'_N\left(\frac{n}{N}\right) \text{sinc}\left(N\left(\ell - \frac{n}{N}\right)\right) \cdot e^{-j2\pi\frac{N-1}{2}\left(\ell - \frac{n}{N}\right)} \right), \quad (11)$$

where the exponential term inside the summation is making sure that the reconstruction is centered at AAL equal to  $\frac{N-1}{2}$ , as seen in Remark 3. One can revert the transformation from the auxiliary NAF response to the NAF response, having  $R_N(\ell) = R'_N(\ell)e^{j2\pi\frac{N-1}{2}\ell}$ . Given the replica generated according to Lemma 2, one could define the minimum set of indexes without replica as  $\mathcal{N}_N = \{n \in \mathbb{Z} : -\frac{N}{2} \leq n < \frac{N}{2}\}$ , and just sample them as follows

$$\begin{aligned} R'_N(\ell) &= \sum_{n \in \mathcal{N}_N} \sum_{k=-\infty}^{+\infty} \text{sinc}\left(N\left(\ell - \frac{n+kN}{N}\right)\right) \\ &\cdot L'_N\left(\frac{n+kN}{N}\right) e^{-j2\pi\frac{N-1}{2}\left(\ell - \frac{n+kN}{N}\right)} = \\ &= \sum_{n \in \mathcal{N}_N} L'_N\left(\frac{n}{N}\right) \cdot \sum_{k=-\infty}^{+\infty} e^{-j2\pi\frac{N-1}{2}\left(\ell - \frac{n+kN}{N}\right)} \\ &\cdot \text{sinc}\left(N\left(\ell - \frac{n+kN}{N}\right)\right). \end{aligned} \quad (12)$$

We show in Appendix C how one can simplify the infinite summation part of (12), obtaining

$$\begin{aligned} R'_N(\ell) &= \sum_{n \in \mathcal{N}_N} L'_N\left(\frac{n}{N}\right) D_N\left(\ell - \frac{n}{N}\right) \\ &\cdot e^{-j2\pi\frac{N-1}{2}\left(\ell - \frac{n}{N}\right)} = \\ &= \sum_{n \in \mathcal{N}_N} L'_N\left(\frac{n}{N}\right) D'_N\left(\ell - \frac{n}{2dN}\right), \end{aligned} \quad (13)$$

which is a convolution of the sampled sequence with Dirichlet kernels with a linear phase component, defined as  $D'_N(\ell) = D_N(\ell)e^{-j\pi(N-1)\ell}$ . The derivation of the reconstructed NAF response can be obtained similarly, with the absence of any linear phase shift in the Dirichlet kernel, making it equivalent to a trigonometric interpolation [20] of the samples taken uniformly in the NAF domain

$$R_N(\ell) = \sum_{n \in \mathcal{N}_N} L_N\left(\frac{n}{N}\right) D_N\left(\ell - \frac{n}{N}\right). \quad (14)$$

We define the following continuous functions corresponding to the angular scans and limited Dirichlet kernel with shifted

phase, respectively

$$\overline{L}'_N(\ell) = \sum_{n \in \mathcal{N}_N} L'_N(\ell) \delta\left(\ell - \frac{n}{N}\right), \quad (15)$$

$$\overline{D}'_N(\ell) = \begin{cases} D'_N(\ell) & \text{if } |\ell| \leq 0.5 \\ 0 & \text{otherwise} \end{cases}. \quad (16)$$

**Theorem 1.** *The reconstructed auxiliary NAF response in (13) is equivalent to a circular convolution of unitary period of the two functions  $\overline{L}'_N(\ell)$  and  $\overline{D}'_N(\ell)$ .*

*Proof.* Using the definition in (15), one can reshape (14) into

$$\begin{aligned} R'_N(\ell) &= \int_{-\infty}^{+\infty} \overline{L}'(\eta) \overline{D}'_N(\ell - \eta) d\eta = \\ &= \overline{L}'(\ell) * \overline{D}'_N(\ell). \end{aligned} \quad (17)$$

Then, given the auxiliary NAF response periodicity, see Lemma 2, one can write the linear convolution (17) as a periodical convolution [26] with unitary period as

$$R'_N(\ell) = \int_{-0.5}^{0.5} \overline{L}'(\eta) \sum_{k=-\infty}^{+\infty} \overline{D}'_N(\ell - \eta - k) d\eta. \quad (18)$$

The previous equation holds since all non-zero elements of  $L'(\ell)$  and  $\overline{D}'_N(\ell)$  lie in  $[-0.5, 0.5)$ , given their definitions in (15)-(16). Therefore, as shown in [26], the periodical convolution is also a circular convolution with unitary period of the two aperiodic functions  $\overline{L}'_N(\ell)$  and  $\overline{D}'_N(\ell)$ .  $\square$

In practical applications, one is not interested in all infinite NAF values but a fine grid in the NAF interval of interest. Therefore, the available samples  $L'_N(nN^{-1})$ ,  $n \in \mathcal{N}_N$ , must be up-sampled by a factor  $U$ , getting all  $R'_N(u(NU)^{-1})$ ,  $u \in \mathcal{N}_{NU}$ . We define the vector  $\overline{\mathbf{I}}'$ , whose elements are  $\overline{\mathbf{I}}'_{n-\underline{N}} = L'_N(nN^{-1})$ , with  $n \in \mathcal{N}_N$  and  $\underline{N}$  being equal to the infimum of  $\mathcal{N}_N$ . One can create the following vectors of  $NU$  elements, spanning the period of the continuous functions defined in (15) and (16), sampled at  $\ell = u/(NU)$

$$\mathbf{I}'_u = \begin{cases} \overline{\mathbf{I}}'_n & \text{if } u = Un, n = 0, \dots, N-1 \\ 0 & \text{otherwise} \end{cases}, \quad (19)$$

$$\mathbf{d}'_u = \overline{D}'_N\left(\frac{u}{NU}\right) = D'_N\left(\frac{u}{NU}\right), \quad (20)$$

where  $u \in \{u \in \mathbb{N}_0 : u < NU\} = \mathcal{U}_{NU}$ .

**Theorem 2.** *The up-sampled auxiliary NAF response can be obtained with a circularly sampled convolution in the NAF domain of the vectors  $\mathbf{I}'$  and  $\mathbf{d}'$  of Equations (19)-(20).*

*Proof.* Theorem 1 states that the desired reconstructed NAF response can be obtained as a circular convolution between  $\overline{L}'_N(\ell)$  and  $\overline{D}'_N(\ell)$ . If the sampling theorem is satisfied, one could perfectly reconstruct the continuous NAF signal, or (up-)sample it. Therefore, the reconstructed up-sampled auxiliary NAF response can be written as the following circular convolution of  $\mathbf{I}'$  with  $\mathbf{d}'$

$$\mathbf{r}'_u = \sum_{v \in \mathcal{U}} \mathbf{I}'_v \mathbf{d}'_{\text{mod}_{NU}(u-v)} \text{ with } u \in \mathcal{U}_{NU}. \quad (21)$$

$\square$

Given the convolution of  $N$  non-zero samples of  $\mathbf{l}'$  with  $NU$  samples of  $\mathbf{d}'$ , the SARA Convolution (SARA Conv.) technique has complexity  $\mathcal{O}(UN^2)$ .

**Lemma 3.** *The inverse DFT transforms with  $NU$  elements ( $IDFT_{NU}$ ) of  $\mathbf{l}'$  and  $\mathbf{d}'$  can be written, respectively, as follows*

$$\mathbf{l}'_A = IDFT_{NU}(\mathbf{l}') = \left[ IDFT_N(\tilde{\mathbf{l}}'), \dots, IDFT_N(\tilde{\mathbf{l}}') \right], \quad (22)$$

$$\mathbf{d}'_A = IDFT_{NU}(\mathbf{d}') = [\mathbf{1}_N, \mathbf{0}_{NU-N}], \quad (23)$$

where  $IDFT_N(\tilde{\mathbf{l}}')$  in (22) is with  $N$  elements and it is repeated  $U$  times sequentially.

*Proof.* The complete proof can be found in Appendix D.  $\square$

**Theorem 3.** *The up-sampled reconstructed auxiliary NAF response can be obtained from  $\tilde{\mathbf{l}}'$  as*

$$\mathbf{r}' = DFT_{NU} \left( \left[ IDFT_N(\tilde{\mathbf{l}}'), \mathbf{0}_{NU-N} \right] \right), \quad (24)$$

corresponding to a DFT interpolation of the auxiliary sampled response.

*Proof.* Since circular convolution in one domain is equivalent to an element-wise multiplication of the IDFT/DFT transforms [26], the SARA DFT-based reconstruction (SARA DFT) of (24) can be obtained from (21) by applying IDFT to both  $\mathbf{l}'$  and  $\mathbf{d}'$ , applying element-wise multiplication (Hadamard product), and finally obtaining the result in the NAF domain with the DFT operation

$$\begin{aligned} \mathbf{r}' &= DFT_{NU} \left( IDFT_{NU}(\mathbf{l}') \odot IDFT_{NU}(\mathbf{d}') \right) = \\ &\stackrel{(22),(23)}{=} DFT_{NU} \left( \left[ IDFT_N(\tilde{\mathbf{l}}'), \dots \right] \odot [\mathbf{1}_N, \mathbf{0}_{NU-N}] \right) = \\ &= DFT_{NU} \left( \left[ IDFT_N(\tilde{\mathbf{l}}'), \mathbf{0}_{NU-N} \right] \right). \end{aligned} \quad \square$$

Accordingly, the resulting complexity is  $\mathcal{O}(NU \log(NU))$  due to the final DFT operation, that however is applied to a vector of only  $N$  non-zero elements.

#### IV. PRACTICAL APPLICATIONS OF SARA

##### A. Omni-directional transmitter and directional receiver

**Algorithm 1** NAF reconstruction with  $N$  elements ULA.

- 
- 1: **procedure** SCAN AND INTERPOLATE
  - 2:  $\tilde{\mathbf{l}}' \leftarrow$  scan  $L_N(\eta)$  (5), with  $\eta \in \mathcal{L}_N^{(\text{Rx})}$  from (25)
  - 3:  $\tilde{\mathbf{l}}' \leftarrow$  sampled auxiliary response (7)
  - 4:  $\mathbf{l}' \leftarrow$  up-sample  $\tilde{\mathbf{l}}'$  (19) only with SARA Conv.
  - 5:  $\mathbf{r}' \leftarrow$  Up-sampled NAF response with SARA Conv. or SARA DFT, using Theorem 2 or 3, respectively
  - 6:  $\mathbf{r} \leftarrow$  Non-auxiliary response, inverting (7)
  - 7: **return**  $\mathbf{r}$
- 

Assuming that the scenario is already illuminated by another device, we want to reconstruct the NAF response by up-sampling a finite angular scan by a factor  $U$ . The reconstruction procedure to get the reconstructed (non-auxiliary) NAF

response  $\mathbf{r}$  is sketched in Algorithm 1. In particular, to obtain the NAF response without the auxiliary AAL translation, one can apply (7) to its available samples  $\tilde{\mathbf{l}}'$ , obtaining the sampled auxiliary response. Then, the auxiliary response can be reconstructed with Theorems 1, 2, or 3, and then (7) can be inverted to get the desired reconstructed NAF response. The NAF to be scanned are

$$\mathcal{L}_N^{(\text{Rx})} = \{nN^{-1} : n \in \mathcal{N}_N\}. \quad (25)$$

##### B. Different number of NAF samples

So far, this work determined that  $N$  angles must be scanned to fully reconstruct the angular response of a ULA with  $N$  elements. In case a number of angular scans  $\bar{N} \neq N$  is available, previous considerations can be modified to make the most out of the available scans. In case more scans are available, i.e.  $\bar{N} > N$ , one could have a finer sampling of the NAF domain, thus sample angles in  $\mathcal{L}_{\bar{N}}^{\text{Rx}}$ . When reconstructing the signal, one should note from (8) that the replica are still generated by the  $N$  elements of the ULA. Therefore, steps similar to (14) and Appendix C could be applied with an  $N$  elements ULA, but sampling the angular domain every  $\bar{N}$ , getting the reconstruction formula for  $\bar{N} \neq N$

$$L'(\ell) = \frac{N}{\bar{N}} \sum_{l \in \mathcal{L}_{\bar{N}}} L_N(l) D_N((\ell - l)). \quad (26)$$

The factor  $N/\bar{N}$  comes from the different normalization factors in (52) of the rectangle with reduced aperture  $\bar{N}$ , whereas the train of impulses retains the same unitary periodicity.

On the other hand, a loss of information is experienced in the reconstructed NAF response if less angles than the necessary amount can be scanned. This can happen due to the resource shortage in the wireless system, or due to the analog beam codebook having a reduced number of total beams that can be stored. However, if the full non-aliased angular unitary aperture is not of interest, one could focus the available  $\bar{N}$  scans in the directions of interest  $\mathcal{D} \subset \mathcal{L}_N^{(\text{Rx})}$ , still sampling the NAF domain with period  $1/N$  and then interpolating, only in the interval spanned by  $\mathcal{D}$ . The missing scans needed for the NAF reconstruction, see (15), can be set to zero, i.e.  $L'_N(\ell) = 0, \forall n \in \mathcal{L}_N^{(\text{Rx})} \setminus \mathcal{D}$ . Minor losses in terms of the reconstructed NAF response's distortion come from not probing the full NAF domain. Note that the response of an angular impulsive scatterer is spread over the full NAF domain aliasing period due to the finiteness of the array aperture. However, this approach allows to preserve the resolution in the directions of interest. Alternatively, if the full NAF domain aliasing period is of interest, one could reduce the number of operating antennas to  $\bar{N}$  contiguous elements and perform the reduced scan accordingly. This results in a reconstructed NAF response with lower resolution, due to the reduced aperture of the operating array. The two approaches above can be trivially combined in case the number of necessary scans is not sufficient to scan a reduced angular range  $\mathcal{D}$ .

##### C. Directional transmitter and receiver

For sensing applications, we may have a transmit array illuminating the environment where beamforming can be applied

both at the transmitter and at the receiver side. Their combined effect can be seen as a multiplication of their responses in the NAF domain, thus a convolution in the AAL domain. This allows us to unify our dissertation with the literature on sum co-array [27], where the achievable Point Spread Function of a transmit and a receive array is defined by their sum co-array. The sum co-array is a virtual array structure defined as the set of pairwise sums of the transmit and receive elements' locations. Note that the convolution in the AAL domain of discrete sequences, whose non-zero elements are at the transmitter's and receiver's locations  $\mathcal{X}$ , is located at the sum co-array's virtual locations. In the particular case of a full duplex ULA with  $N$  elements, it is straightforward to show that the sum co-array is a ULA with  $2N - 1$  elements. Therefore, one should operate as if a  $2N - 1$  ULA were available to perform SARA. Note the almost doubled resolution, which is due to the joint efforts of transmitter and receiver.

#### D. Extension to URA

Similar techniques can be extended to 2D arrays to obtain angular estimates in both azimuth and elevation. In particular, one could generalize the one-dimensional SARA considerations tailored for ULA to URA. We assume an  $N \times M$  URA structure with vertical (z axis) and horizontal (x axis) antenna spacing corresponding to  $d_1$  and  $d_2$ , respectively. Its angular response at elevation  $\phi$  and azimuth  $\theta$  can be written as [28]

$$L_{N,M}(\phi, \theta) = \sum_{n=0}^{N-1} \sum_{m=0}^{M-1} a_{n,m} e^{-j2\pi(z'_n \frac{d_1}{\lambda} \sin(\phi) + x'_m \frac{d_2}{\lambda} \frac{\sin(\theta)}{\cos(\phi)})}, \quad (27)$$

where  $z'_n$  is the  $n$ -th antenna location in the vertical AAL axis. We recall the constraint of  $|\phi| + |\theta| \leq \pi/2$  in spherical coordinates. From (27) we notice that the vertical phase shift depends on a vertical NAF  $\eta = \frac{d_1}{\lambda} \sin(\phi)$ , whereas the horizontal phase shift on a horizontal NAF of  $\ell = \frac{d_2}{\lambda} \sin(\theta) / \cos(\phi)$ . Since the horizontal NAF depends on the elevation, the physical azimuth and elevation cannot be decoupled and are obtained from the NAF dimensions as

$$\phi(\eta) = \sin^{-1} \left( \frac{\lambda}{d_1} \eta \right), \quad (28)$$

$$\theta(\ell, \eta) = \sin^{-1} \left( \frac{\lambda}{d_2} \cos(\phi(\eta)) \ell \right). \quad (29)$$

With procedures similar to the ones shown in Section III, one can demonstrate that these two NAF dimensions are the (orthogonal) Fourier dual of the vertical and horizontal AAL axes. Accordingly, all theorems in Section III can be extended for the 2D case. Therefore, the full 2D NAF response can be obtained by performing  $NM$  scans along directions given by the vertical and horizontal NAF sets given by

$$\mathcal{L}_{N,M}^{(Rx)} = \{\eta = nN^{-1}, \ell = mM^{-1} : n \in \mathcal{N}_N, m \in \mathcal{N}_M\}, \quad (30)$$

where (28)-(29) can be used to determine the corresponding elevation and azimuth angles. The 2D angular reconstruction

can be obtained by convolving the scan with the following 2D Dirichlet kernel

$$D_{N,M}(\eta, \ell) = D_N(\eta) \cdot D_M(\ell), \quad (31)$$

whose inputs are the vertical and horizontal NAFs, respectively. Accordingly, Theorems 1, 2 and 3 can be extended to cover the 2D angular space. Regarding the sensing applications mentioned in Subsection IV-C, the role of the sum co-array structure still holds when a transmitting and a receiving URA operate together. In case of a co-located URA with  $N \times M$  elements, one still has a  $(2N - 1) \times (2M - 1)$  URA structure determining the performance and features of SARA.

## V. NUMERICAL EXPERIMENTS

### A. Simulation Setup

In our simulation experiments, a single terminal sensing scenario with full duplex capabilities is considered, equivalent to mono-static radar. The array consists of a horizontal  $N$ -element analog ULA with a corresponding sum co-array of  $2N - 1$  elements. The antennas experience the same additive white Gaussian noise (AWGN) power  $\sigma_n^2$  and are separated by  $d = \lambda/2$ , making the non-aliased unitary period of the NAF axes correspond to the  $[-\pi/2, \pi/2]$  angular interval. Therefore, after receive combining of the  $N'$  available scans  $\eta_1, \dots, \eta_{N'}$  as in (5), the available scan vector can be written as

$$\bar{\mathbf{l}}_{(\text{NA})} = [L_N(\eta_1), \dots, L_N(\eta_{N'})] + \mathbf{n}, \quad (32)$$

where the variance of each AWGN sample in the row vector  $\mathbf{n}$  is

$$\sigma^2 = \frac{1}{N^2} \sum_{j=0}^{N-1} \sigma_n^2 = \frac{1}{N} \sigma_n^2, \forall i. \quad (33)$$

Hereafter, for ease of notation, we drop the number of sum co-array elements from the ideal angular response and received noisy response, leading to  $L(\eta)$  and  $R(\eta)$ , respectively.

We place point scatterers in the environment such that their path losses and reflection coefficients are of unitary gain. Note that the estimation of few impulsive scatterers in the NAF (or angular) domain, with their complex coefficients, coincides with channel estimation of narrowband mmWave and higher carrier frequency wireless channels, see for instance [7]. The extension to broadband signals, thus requiring to estimate also the delays of the scatterers, will be subject to future work. Our findings could be extended to more general cases of imaging, apart from the fact that performance, like object resolution, is more difficult to measure. Assuming unitary power transmission, one could assess the performance impact with an equivalent signal to noise ratio (SNR)

$$\gamma = \sigma^{-2} = N\sigma_n^{-2}. \quad (34)$$

Note that the factor  $N$  corresponds to beamforming gain of the receive array. The  $Q$  targets are placed randomly at angles in the  $[-\theta^{\max}, \theta^{\max}]$  interval. Due to the typical 120 degrees sector considered in deployments, we default to  $\theta^{\max} = 60$  degrees. In some results, targets move at a constant speed of  $\nu$  m/s, with a uniform random orientation with respect to the

array, generating Doppler shifts due to acquisitions taken at different times.

Angles are scanned by steering both transmit and receive beamforming weights at the same angle, that changes at each acquisition. Given the  $2N-1$  elements of the sum co-array, a minimum of  $2N-1$  angles must be scanned. By default, the scanned angles are sampled uniformly in the NAF, but we also evaluate the performance of uniform sampling in the angular domain. The angular sweeping is executed sequentially from the lowest NAF value to the highest, with scan period  $P_S$ . For the single target scenario, the target's NAF location is estimated by up-sampling the angular response to 512 points and determining the location of its absolute value maximum. The estimate is further refined by determining the maximum's location of the parabola passing through the first determined maximum and its two neighbor points.

The investigated algorithms for up-sampling the NAF response are

- The SARA DFT proposal of Theorem 3, with  $N' = 2N - 1$  NAF samples.
- A CUBIC Hermite spline, which is a local interpolation using third-degree ( $P=3$ ) polynomials that forces continuity on the interpolation's derivatives [29], using  $N' = 2N - 1$  NAF samples. We chose this baseline due to its comparable computational complexity and better performance compared to other orders.
- The ‘‘SARA - Red’’ (reduced), where we instead used only  $N' = N$  samples.

We also compare the NAF estimation performance with the MUSIC algorithm [22]. The vector  $\hat{\mathbf{a}}$  containing the complex signal at each of the  $2N-1$  elements of the sum co-array can be estimated with the following minimum mean square error (MMSE) estimate [30] as follows

$$\bar{\mathbf{I}}_{(\text{NA})} \stackrel{(5)}{=} \underbrace{\begin{bmatrix} a_0 & \dots & a_{2N-1} \end{bmatrix}}_{\mathbf{a}} \underbrace{\begin{bmatrix} e^{-j2\pi x'_0 \eta_1} & \dots & e^{-j2\pi x'_0 \eta_{2N-1}} \\ \vdots & \ddots & \vdots \\ e^{-j2\pi x'_{2N-1} \eta_1} & \dots & e^{-j2\pi x'_{2N-1} \eta_{2N-1}} \end{bmatrix}}_{\mathbf{S}}$$

$$+ \mathbf{n} \Rightarrow \quad (35a)$$

$$\hat{\mathbf{a}} = \bar{\mathbf{I}}_{(\text{NA})} \mathbf{S}^H (\mathbf{S} \mathbf{S}^H + \sigma_n^2 \mathbf{I}_{2N-1})^{-1}. \quad (35b)$$

Note that the steering matrix  $\mathbf{S}$  is a full rank square matrix with equal eigenvalues, when  $2N - 1$  scans in  $\bar{\mathbf{I}}_{(\text{NA})}$  are taken uniformly in NAF. The multiple target search with MUSIC is performed as in Section III-B/C of [31].

For the single target simulations, a single angle is estimated. On the other hand, in experiments with multiple targets, we estimate the number of scatterers  $Q$  with the minimum description length (MDL) criterion [32] of the computed eigenvalues during MUSIC.

The complexity of CUBIC interpolation is  $\mathcal{O}(NU)$  if the upsampling factor is much greater than the reconstruction order squared, i.e.  $U \gg P^2$ , otherwise  $\mathcal{O}(NP^2)$  [33]. The computational effort of MUSIC is dominated by the evaluation of the MUSIC spectrum, for which evaluating a single point exhibits cubic complexity with respect to  $2N-1$ . However, to not miss any targets, the sampling granularity of the spectrum

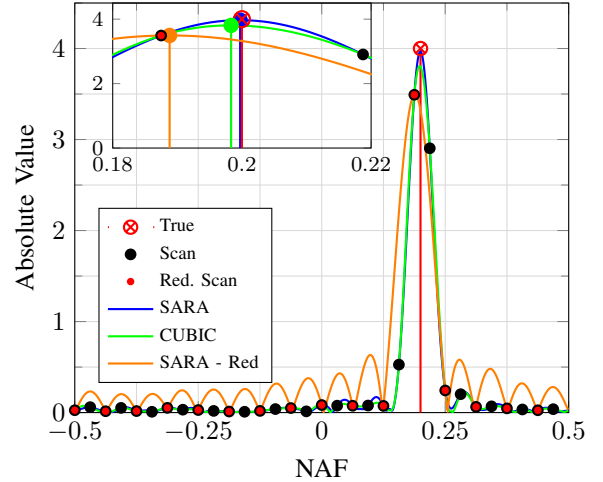


Fig. 2: Example of angular scan and reconstruction with a single target at NAF  $\ell = 0.2$  without noise, where ‘‘SARA - Red’’ uses half of the angular scans compared to SARA and CUBIC.

should be based on the resolution, requiring at least  $2N-1$  evaluations, and thus resulting in  $\mathcal{O}(N^4)$ . Accordingly, the asymptotic complexity of the considered algorithms can be found in Table I. One should note, however, that in our experiments we have observed almost an order of magnitude reduction in execution time of the SARA DFT for all the considered values of  $N$  and  $U$  compared to CUBIC. On the other hand, the MUSIC super-resolution baseline show a larger scaling of the asymptotic behavior and a several orders of magnitude higher execution time in our numerical studies.

Unless mentioned otherwise, the default parameters used in every figure are recapped in Table II. The scan period of  $8.93 \mu\text{s}$  is due to the symbol length of 120 kHz sub-carrier spacing, that is used at the 28 GHz frequency bands [34]. An example of angular scan and reconstruction from a noiseless acquisition of a single target at NAF  $\ell = 0.2$  can be found in Fig. 2, where we plot the absolute values of the scan with points and the reconstruction curves, highlighting their maximum points. For this figure, we chose a number of scans equal to  $2N$  for SARA and CUBIC, to allow angular samples of SARA - Red (which only uses  $N$  scans) to be in the same position as the other two alternatives. Note how the SARA (blue) maximum is on top of the true target's (red) NAF position and amplitude, whereas the CUBIC reconstruction in green introduces some distortion. Finally, we have ‘‘SARA - Red’’ using only half of the angular scans that reconstructs the NAF response with Dirichlet kernels with larger main lobe  $B_N^{-1}$  half width - instead of  $B_{2N-1}^{-1}$  - and order  $N$ . As shown earlier, this introduces aliasing in the AAL. Therefore, the reconstructed response of ‘‘SARA - Red’’ has a maximum with some displacement both in NAF and amplitude with respect to the true target.

### B. Reconstruction results - Single target

In this subsection, we analyze the performance of angular estimation when a single target is present in the environment.

TABLE I: Asymptotic complexity of the considered algorithms

SARA DFT	SARA Conv.	CUBIC	MUSIC
$\mathcal{O}(NU \log_2(NU))$	$\mathcal{O}(N^2U)$	$\max(\mathcal{O}(NU), \mathcal{O}(NP^2))$	$\mathcal{O}(N^4)$

TABLE II: Default simulation parameters

Base station antennas $N$	16 vertically polarized
Central frequency (wavelength $\lambda$ )	28 GHz (10.71 mm)
Antenna separation $d$	$\lambda/2$
Scan period $P_S$	8.93 $\mu$ s
Target speed $\nu$	0 m/s
Maximum target's angle $\theta^{\max}$	$\pi/3$ rad. (60 deg.)

This allows to assess the capability of different algorithms without interference by additional targets, being impacted only by the AWGN and the algorithm itself.

a) *NAF root mean square error (RMSE) with variable  $N$* : The RMSE of a single target's NAF estimate is plotted in Fig. 3 with  $N = 16, 128$ . Note that the noise power axis is plotted in reverse order, corresponding to having plots with increasing SNR on the x axis. The other parameters are according to Table II. Given the NAF period of  $2d/\lambda = 1$ , the NAF errors are wrapped modulo 1 operations, determining the NAF RMSE as follows

$$\text{NAF RMSE} = \sqrt{E_j \left[ \left| \text{mod}_1(\eta_j - \hat{\eta}_j) \right|^2 \right]}, \quad (36)$$

where  $\eta_j, \hat{\eta}_j$  are the true and estimated NAF in the  $j$ -th experiment, respectively. Given that the signal model at each antenna (2) coincides with a complex sinusoid, the problem of NAF estimation can be seen as frequency estimation, given  $N$  observations of a flat noisy channel. Therefore, assuming here to have access to the signal at each antenna element, which is possible only with digital beamforming capabilities, we can write the RCA, see equation (26) of [23].

$$\text{RCA} = \frac{1}{2\pi\sigma_n} \sqrt{\frac{6}{N(N^2 - 1)}}. \quad (37)$$

In contrast to typical angle of arrival bounds, RCA does not depend on the incoming angle, given the NAF transformation representing the Fourier domain of the ULA's antenna locations.

Among the sampling and reconstruction algorithms, SARA outperforms both CUBIC and "SARA - Red". The latter is clearly suboptimal and will not be further evaluated. It exhibits a noise floor and is unable to capture the true characteristic of the NAF response in its reconstruction. Even if the RCA (37) is only an approximation of the lower bound on the performance of fully digital systems, we can note how SARA approaches RCA curves at high SNR, exhibiting a linear behavior with  $\sigma_n^{-1}$ . This is a further validation point for SARA, which allows to achieve the same NAF RMSE of the RCA, as if digital beamforming were possible. However, this behavior starts to decline at extremely low RMSE, due to NAF quantization errors present in the up-sampled reconstruction with 512 points, instead of an ideal continuous function.

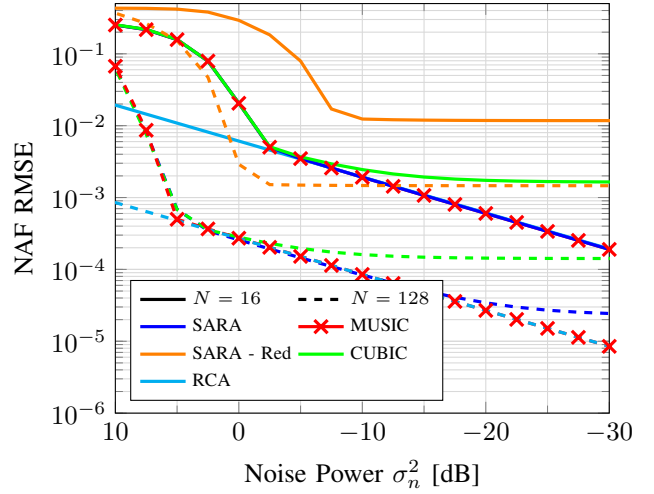


Fig. 3: RMSE of single target NAF estimation using ULAs with variable number of antennas.

As a super-resolution method, MUSIC can deliver similar performance as SARA at low SNR and approach the RCA at high SNR. We can notice similar behavior with  $N = 16$  and  $N = 128$ , where having more antennas simply allows to reduce the RMSE. From the discussion of this paragraph, in what follows, we choose CUBIC and MUSIC as our most interesting baselines. The first compares SARA against another reconstruction algorithm, the latter against a super-resolution method.

b) *Target's peak amplitude RMSE with variable  $N$* : The RMSE of the peak estimation error is plotted in Fig. 4 for the considered reconstruction algorithms, i.e. SARA and CUBIC, and it is defined as

$$\text{Peak RMSE} = \sqrt{E_j \left[ \left| L(\eta_j) - R(\hat{\eta}_j) \right|^2 \right]}, \quad (38)$$

where  $R(\hat{\eta}_j)$  is the amplitude of the up-sampled reconstructed response, with the additional quadratic interpolation, as described in Subsection V-A. SARA gains in high SNR regimes, due to the absence of error floors, apart from the ones given by the reconstruction quantization, occurring at much lower Peak RMSE values. Note that the noise power at which the two curves detach increases with the number of antennas.

c) *The effect of user speed  $\nu$* : We analyze in Fig. 5 the sensitivity with respect to target's speed  $\nu$ . Note that the higher the speed values, the worse the performance degradation. Also in this case, the performances of SARA and MUSIC overlap, while CUBIC exhibits a much higher error floor.

d) *The effect of different angular sampling*: In this paragraph, we investigate the NAF estimation losses due to sub-optimal uniform angular sampling, as done in [17] - not

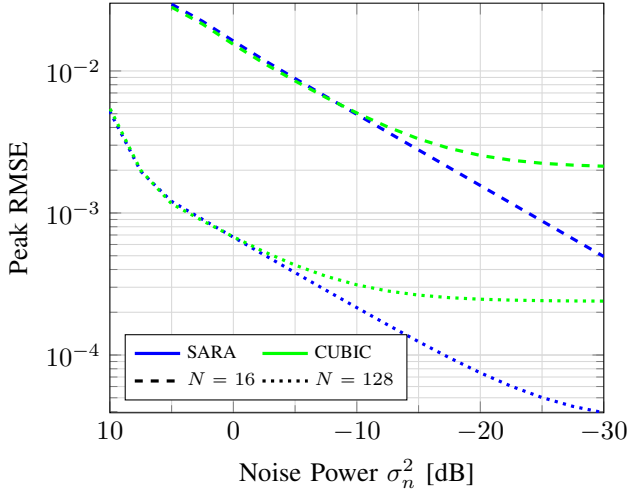


Fig. 4: RMSE of single target peak estimation with variable number of antennas.

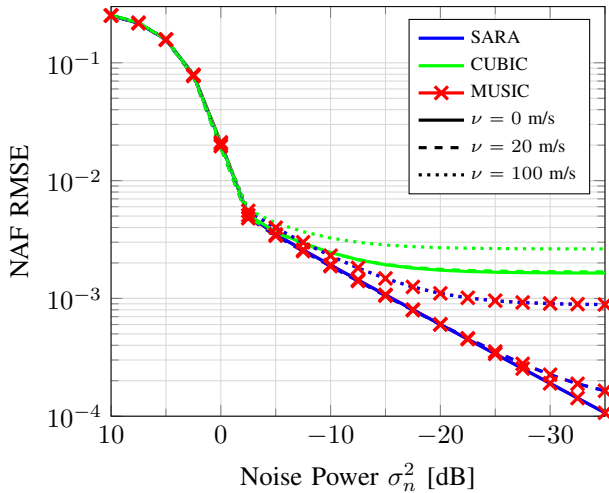


Fig. 5: RMSE of single target NAF estimation with target speed  $\nu = \{0, 20, 100\}$  m/s.

in NAF - in the following set

$$\mathcal{D}_{2N-1} = \left\{ \theta = \frac{n\pi}{N} : n \in \mathcal{N}_{2N-1} \right\}. \quad (39)$$

The reconstruction is done working in the angular axes, leveraging Theorem 3 (not in NAF as stated in the theorem) for SARA and simple cubic interpolation for the CUBIC case, whereas the signal at each antenna element for MUSIC is still estimated with (35b). We compare the “Angle” option versus the optimal uniform NAF sampling of angles from the set  $\mathcal{L}_{2N-1}$ , according to (25), and reconstruction done in the NAF domain.

Fig. 6 shows an example of uniform NAF and angular sampling with 8 samples. Note that NAF sampling focuses more on angles close to zero (array’s boresight), allowing to achieve higher resolution at these angles. This is in line with the well-known property of ULAs to have stronger resolution capabilities at boresight. In Fig. 7 we plot the NAF estimation RMSE for the two angular sampling criteria defined earlier.

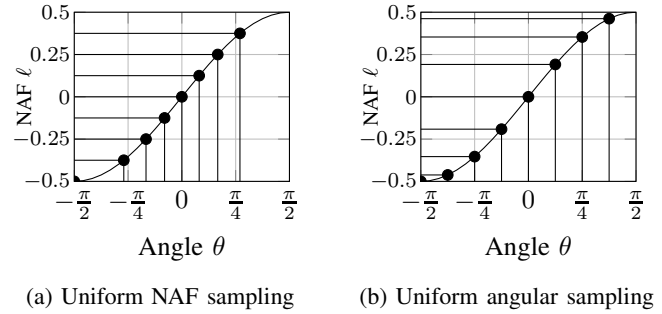


Fig. 6: Example of uniform sampling of NAF (a) and angular (b) domain with 8 samples. The plotted curve is the transformation between NAF and angular domain  $\ell = \frac{d}{\lambda} \sin(\theta) = \sin(\theta)/2$ .

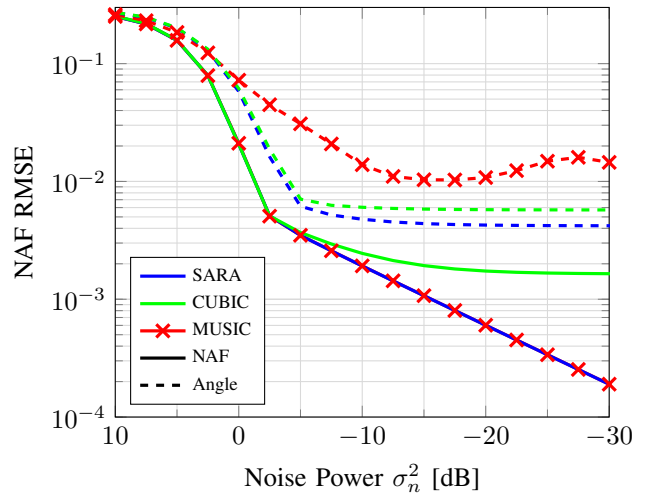


Fig. 7: RMSE of single target NAF estimation with uniform sampling of NAF and angles.

One can observe the error floors of dashed “Angle” curves, implying that sampling angles uniformly in the angular domain leads to performance losses. The performance gap is more remarkable with MUSIC compared to the other two considered algorithms, due to the difficulty of equalizing the steering vector matrix  $\mathbf{S}$  in (35) if the  $2N - 1$  sampled angles are not uniform in NAF.

*e) The impact of additional scans:* Additional angular acquisitions on top of the minimum  $2N - 1$  can be considered to reduce the impact of poor angular sampling choices, see the Angle curves of Fig. 7. For example, in Fig. 8 the NAF estimation RMSE is plotted versus the number of scans used minus  $2N - 1$ . The curves are for different noise powers 0 dB and  $-20$  dB and angular sampling techniques, i.e. the NAF and Angle uniform sampling introduced in the previous paragraph.

As one could anticipate, the RMSE diminishes with additional scans. However, the performance of the optimal “SARA - NAF” (and the overlapping “MUSIC - NAF”) improves only slightly since the signal was not experiencing any distortion in the reconstruction according to Theorem 3. Therefore, the additional angular samples just increase the SNR, as described in Subsection IV-B. On the other hand, the gains in all the

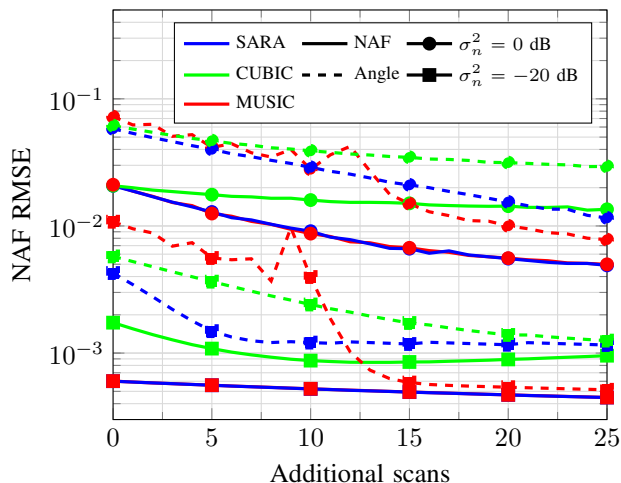


Fig. 8: RMSE of single target NAF estimation versus the number of additional scans over the minimum number of  $2N - 1 = 31$ . Curves are with uniform sampling of NAF and angles, and with different noise power  $\sigma_n^2 = \{0, -20\}$  dB.

other options are larger, thanks to the increased number of samples taken close to boresight, i.e.  $\ell = 0$ , that is where NAF samples the angular domain more frequently compared to Angle. Focusing on the low noise case, i.e.,  $\sigma_n = -20$  dB, we see that “SARA - Angle” and “CUBIC - Angle” still exhibit an error floor. On the other hand, after ca. 15 additional scans (50% more) the MMSE equalizer in (35b) seems to finally be able to properly equalize  $\mathbf{S}$ , allowing the MUSIC Angle curve to approach the overlapping “SARA - NAF” and “MUSIC - NAF” curves.

### C. Reconstruction results - Multiple targets

In this subsection, we consider experiments with  $Q = 3$  targets placed at random angles, but spaced by at least  $\Delta\ell$  in the NAF domain. Therefore, for the reconstruction techniques (SARA and CUBIC), we assume that a target is present if the angular response’s magnitude exceeds the constant false alarm rate (CFAR) threshold given by

$$\zeta = \sqrt{-\sigma^2 \ln(1 - (1 - P^{(\text{FA})})^{\frac{1}{2N-1}})}, \quad (40)$$

where  $P^{(\text{FA})}$  is the desired false alarm probability, defined as the likelihood of erroneously detecting a target in the response [35]. For the derivation of (40), please refer to Appendix E. In our study, we chose  $P^{(\text{FA})} = 10^{-3}$ . Note that we also consider a detected peak a false alarm if it is further away from a true target than the Dirichlet kernel’s main lobe half width of  $1/(2N - 1)$ , corresponding to the Rayleigh criterion for the resolution of two targets [36]. The reconstructed angular response is iteratively scanned for the strongest peak. We coherently remove the  $i$ -th iteration’s target contribution to get the angular response for the next iteration as

$$R_{i+1}(l) = R_i(l) - R_i(\hat{\eta}_i) \cdot (D_N(\ell - \hat{\eta}_i))^2, \quad (41)$$

where  $\hat{\eta}_i$  is the NAF estimate of the  $i$ -th iteration’s target. Notice the squaring of  $D_N(l)$ , which is due to the multiplying effects of transmitter and receiver (see Subsection IV-C). However, canceling peaks generated by multiple interfering targets may create false residual peaks at iterations  $i > 1$ . Their detection is prevented by rejecting peak estimates if there was no peak in the original  $R_1(l)$ ,  $l \in [\hat{\eta}_i - 1/(2N - 1), \hat{\eta}_i + 1/(2N - 1)]$ . Finally, sidelobes and inter-target interference can cause additional detections, especially in low-noise scenarios where  $\zeta^{(\text{CFAR})}$  is low. To account for this, the threshold is updated after the first peak’s detection as

$$\zeta' = \max \left\{ \zeta, \kappa \cdot S_N \cdot R_1(\hat{\eta}_1) \right\}, \quad (42)$$

where  $S_N$  is the first sidelobe’s relative amplitude of the used Dirichlet kernel [36], and  $\kappa$  a scaling factor chosen based on experiments and tuned such that the desired  $P^{(\text{FA})}$  can be approximately attained. We found  $\kappa = 6$  to be a suitable value in our scenario. On the other hand, for MUSIC, the peak search routine returns the  $\hat{Q}$  strongest peaks, where  $\hat{Q}$  is estimated with the MDL criterion [32].

Fig. 9 shows probability of false alarm  $P^{(\text{FA})}$ , probability of missed detection  $P^{(\text{MD})}$ , defined as the percentage of undetected targets, and NAF RMSE with  $N = 16$  and  $N = 128$ . We compare our proposal SARA with uniform NAF sampling against CUBIC and MUSIC, with uniform sampling either in NAF or angular domain (“Angle”), respectively. Each curve is evaluated at noise powers  $\sigma_n^2$  of  $-5$  dB and  $-30$  dB. The vertical curves at  $\Delta\ell = 1/(2N - 1)$  representing the Rayleigh criterion for the resolution of two targets are also added.

Observing the  $P^{(\text{FA})}$  curves in the first column of Fig. 9, it can be seen that, due to the imperfect model order estimation with MDL, using MUSIC leads to a higher number of false detections than the reconstruction techniques “SARA - NAF” and “CUBIC - NAF”, which exhibit comparable false alarm rates. In low-noise scenarios, using uniform NAF sampling generally prevents false alarms for high enough  $\Delta\ell$ , whereas uniform sampling in the angular domain can lead to uncontrollable false alarm rates. The  $P^{(\text{MD})}$  curves in Figs. 9b and 9e show that MUSIC, thanks to its super-resolution properties, offers advantages in terms of resolving closely spaced targets in high SNR regimes. Between the reconstruction techniques, “SARA - NAF” offers minor, but consistent resolution gains compared to “CUBIC - NAF”. Also here, the benefits of sampling the NAF domain uniformly are visible, as “CUBIC - Angle” and “MUSIC - Angle” exhibit significantly higher missed detection probabilities than their respective NAF counterparts. Finally, the NAF RMSE curves (rightmost column of Fig. 9) display similar patterns compared to the previously analyzed  $P^{(\text{MD})}$  results. Nonetheless, “SARA - NAF” achieves the lowest RMSE error floor for high target separation, even though giving up some resolution capability with respect to MUSIC in low-noise regimes at small  $\Delta\ell$ . It is further important to highlight that high-noise ( $\sigma_n^2 = -5$  dB) impacts MUSIC the most, especially for  $N = 16$ , where its capability diminishes significantly, while both reconstruction techniques “SARA - NAF” and “CUBIC - NAF” still perform reasonably well.

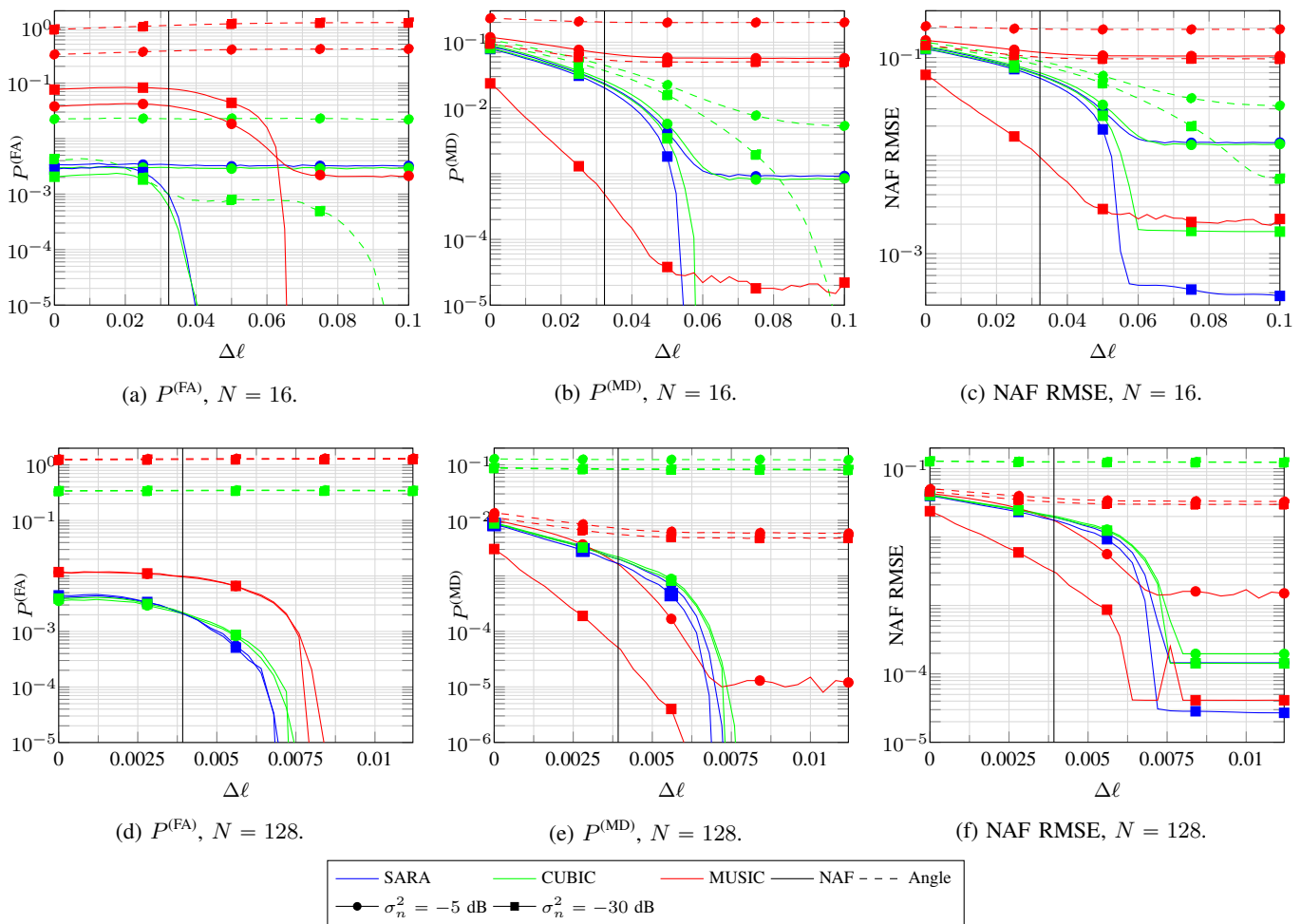


Fig. 9: Probability of false alarm, probability of missed detection, and NAF RMSE of a scenario with three targets and increasing minimum NAF spacing between them. All SARA curves are with uniform sampling in the NAF domain (solid), while for CUBIC and MUSIC also uniform sampling of the angles is considered (dashed). The different noise powers  $\sigma_n^2 = \{-5, -30\}$  dB are marked with circles, and squares, respectively. The vertical lines indicate the Rayleigh criterion for resolution at  $\Delta\ell = 1/(2N - 1)$ .

#### D. 2D imaging example

We conclude the numerical evaluations in this paper by providing a 2D imaging example in Fig. 10. Along the lines of [10] and similar works, we consider the worst-case scenario of an object with  $Q$  independent and identically distributed (i.i.d.) point scatterers, each following a complex normal distribution:  $\mathcal{CN}\left(\frac{1}{\sqrt{2Q}}, \frac{1}{\sqrt{2Q}}\right)$ . In our considered example, the true shape can be found in Fig. 10a, where  $Q = 5017$  and we plot axes in the NAF domain.

Assuming that no noise is present, we assume to illuminate the area with an omni-directional signal, allowing us to focus on the receiver's impact only. A  $16 \times 16$  URA with antenna spacing  $d = \lambda/2$  is considered. The limited aperture of the array generates a loss of resolution, as illustrated in Section II. This is visible in Fig. 10b, where the absolute value of the response of the array is plotted, scanning the azimuth and elevation NAF pairs - or 2D angle -  $\eta$  in the set  $\mathcal{L}_{160,160}^{(\text{RX})}$  defined in (30). This means that a total of 25600 samples is required. In practical wireless systems, this is undesired for the

great consumption of wireless resources needed to perform so many scans. Moreover, if we considered the scenario of Table II, this would require a full scan acquisition time in the order of hundreds of milliseconds, that would generate phase distortions in dynamic scenarios, impacting the accuracy of the reconstruction, as seen in V-B, paragraph c).

Therefore, we sample the response at  $16 \times 16$  2D angles  $\eta \in \mathcal{L}_{16,16}^{(\text{RX})}$ , producing the low-resolution sampled response shown in Fig. 10c. Then, applying what was discussed in Subsection IV-D, we can derive the Dirichlet kernel, plotted in Fig. 10d, and use it to upsample the 2D image by a factor 10. Comparing the initial  $160 \times 160$  scan of Fig. 10b and the reconstructed response in Fig. 10e, one can notice that they are exactly the same. For comparison, also the reconstruction obtained by cubic interpolation is shown in Fig. 10f, where the distortion introduced is clearly visible. In particular, defining

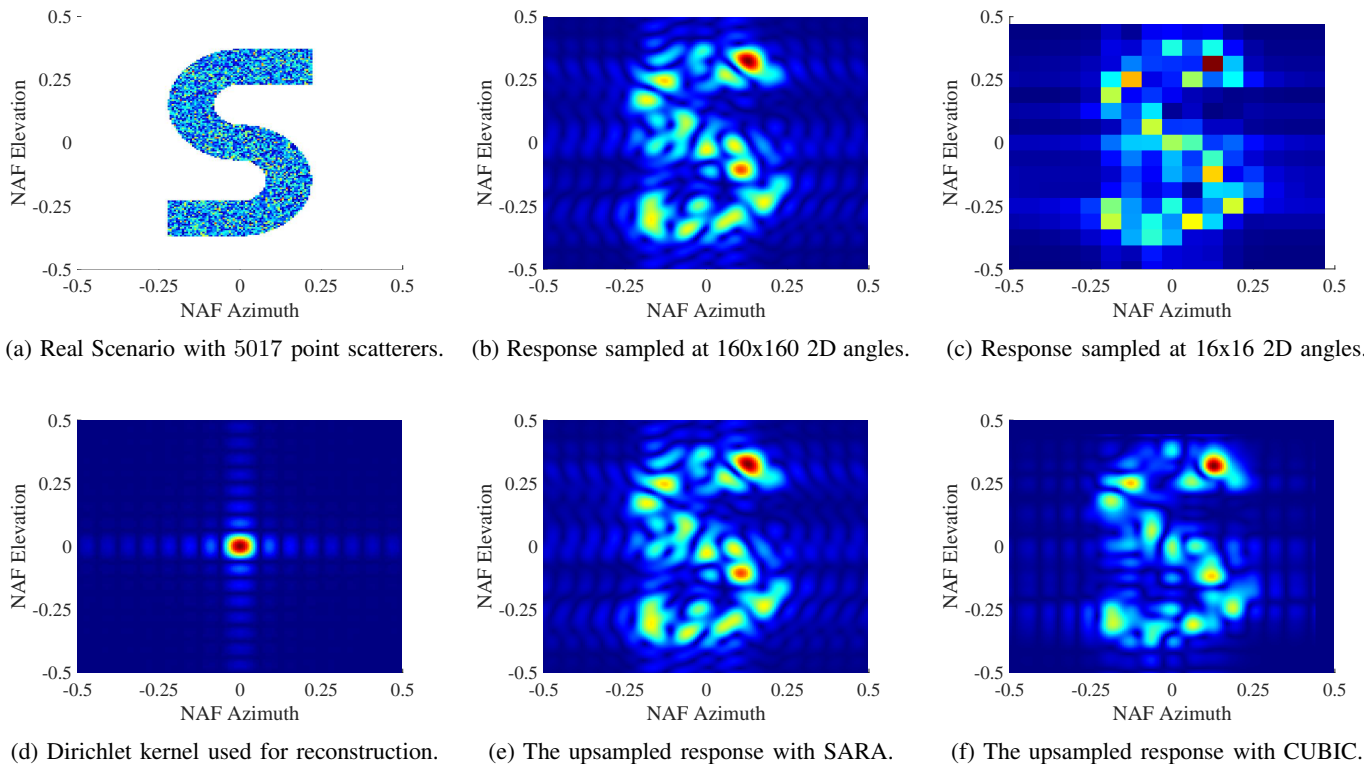


Fig. 10: Example of imaging with a receiver consisting of a 16x16 elements URA and  $d = \lambda/2$ , with omni-directional scenario illumination. All figures plot the magnitude of the respective quantity in jet scale (blue lower values, red higher values). The real scenario is distorted by the limited aperture of the array, that is sampled with a fine (160x160 2D angles) and a coarse (16x16 2D angles) grid. Then, a Dirichlet kernel is used to interpolate the coarse scan, upsampling it to 160x160 with SARA. For comparison, also the result of cubic interpolation is shown.

the normalized RMSE of the reconstruction as

$$\epsilon = \sqrt{\frac{\sum_{\boldsymbol{\eta} \in \mathcal{L}_{160,160}^{(R_x)}} |R(\boldsymbol{\eta}) - L(\boldsymbol{\eta})|^2}{\sum_{\boldsymbol{\eta} \in \mathcal{L}_{160,160}^{(R_x)}} |L(\boldsymbol{\eta})|^2}}, \quad (43)$$

we obtained  $\epsilon^{(\text{SARA})} = 0$  and  $\epsilon^{(\text{CUBIC})} \approx 40\%$  with SARA and cubic reconstruction, respectively.

## VI. CONCLUSION

This paper provided the necessary theory to perfectly sample and reconstruct the angular response (SARA) of ULA and URA. This is a problem of particular relevance when operating with analog and hybrid arrays, that requires to focus on specific angle(s) at each signal transmission/reception. The minimum number and the set of angles to be scanned have been derived, and the Whittaker-Shannon interpolation theorem has been leveraged to demonstrate that the perfect reconstruction of the full angular response of the array coincides with a proper trigonometric interpolation in the normalized angular frequency. Extensions to cases with more or fewer scans, as well as practical applications of theory to sensing use cases are provided, elaborating on the particular case of a full duplex transmit and receive array system.

The performance of the SARA proposal has been evaluated against prior art angular sampling and reconstruction techniques, on angular estimation tasks of single and multiple

targets. SARA consistently outperforms the reconstruction baseline solutions investigated, achieving similar performance as the super-resolution MUSIC algorithm for single impulsive target angular estimation, with the additional advantage of important savings in computational complexity. Moreover, our proposed DFT-based interpolation lowers the required complexity of interpolation below the sub-optimal cubic spline baseline, without any distortion in the reconstruction. We have shown that SARA even approaches the Cramér-Rao lower bound approximation of angular estimation achievable with fully digital beamforming at high SNR.

When considering multiple targets, SARA improves the NAF RMSE at high target separation compared to reconstruction and super-resolution baselines, especially at high SNR. For closer targets, MUSIC offers better resolution capabilities due to its super-resolution properties, but experiences higher false alarm rates and exhibits a severe performance degradation in mid to high noise scenarios. Compared to the cubic reconstruction algorithm, SARA yields gains with regard to multi-target resolution and NAF RMSE, while keeping false alarms at an arbitrary desired level.

In our 2D imaging example, SARA's perfect sampling and reconstruction can avoid the distortion induced by other baselines, which experiences a normalized RMSE of 40%.

In future work, we plan to leverage SARA to showcase its imaging capabilities in an ISAC proof of concept, that

extends current 5th generation (5G) hardware deployments by incorporating radar capabilities. Moreover, we plan to extend the considerations done in this work for narrowband signals to a broadband signal model.

#### ACKNOWLEDGMENTS

The authors want to thank Stefan Wesemann, Thorsten Wild and Traian Emanuel Abrudan for their helpful suggestions, insights, and technical discussions.

#### APPENDIX A PROOF OF LEMMA 1

The NAF response of an incident planar wave with NAF  $\eta = 0$  is

$$L_N(\ell, \eta) = \frac{1}{N} \sum_{n=0}^{N-1} a_n(0) e^{-j2\pi \frac{x_n}{d} \ell} = \frac{1}{N} \sum_{n=0}^{N-1} e^{-j2\pi \frac{x_n}{d} \ell}. \quad (44)$$

One can substitute (1) into (44), having that

$$L(\ell, 0) = \frac{1}{N} e^{j2\pi \frac{N-1}{2} \ell} \sum_{n=0}^{N-1} e^{-j2\pi \ell n}. \quad (45)$$

Leveraging the known formula on truncated geometric series, we have

$$\begin{aligned} b \sum_{n=0}^{N-1} r^n &= b \frac{1-r^N}{1-r} = b \frac{r^{\frac{N}{2}}}{r^{\frac{1}{2}}} \cdot \frac{r^{-\frac{N}{2}} - r^{\frac{N}{2}}}{r^{-\frac{1}{2}} - r^{-\frac{1}{2}}} = \\ &= br^{\frac{N-1}{2}} \frac{r^{-\frac{N}{2}} - r^{\frac{N}{2}}}{r^{-\frac{1}{2}} - r^{-\frac{1}{2}}}. \end{aligned} \quad (46)$$

Note that (46) is equivalent to (45) with  $b = N^{-1} e^{j2\pi \frac{N-1}{2} \ell}$  and  $r = e^{-j2\pi \ell}$ . Note that  $br^{\frac{N-1}{2}} = N^{-1}$ , thus

$$\begin{aligned} L(\ell, 0) &= \frac{1}{N} \frac{e^{+j2\pi \ell \frac{N}{2}} - e^{-j2\pi \ell \frac{N}{2}}}{e^{+j2\pi \ell \frac{1}{2}} - e^{-j2\pi \ell \frac{1}{2}}} = \frac{\sin(2\pi \ell \frac{N}{2})}{N \sin(2\pi \ell \frac{1}{2})} = \\ &= \frac{\sin(\pi N \ell)}{N \sin(\pi \ell)}. \end{aligned} \quad (47)$$

We now consider a generic NAF  $\eta$

$$L_N(\ell, \eta) = \frac{1}{N} \sum_{n=1}^N a_n(\eta) e^{-j2\pi \frac{x_n}{d} \ell} = \frac{1}{N} \sum_{n=0}^{N-1} e^{-j2\pi \frac{x_n}{d} (\ell - \eta)}. \quad (48)$$

One can immediately notice that (48) is the translation of (44) by a term  $\eta$ , therefore

$$L_N(\ell, \eta) = \frac{\sin(\pi N(\ell - \eta))}{N \sin(\pi(\ell - \eta))}. \quad (49)$$

#### APPENDIX B PROOF OF LEMMA 2

One can use (7) to expand the array response as follows

$$\begin{aligned} L'_N(\ell - k) &= \frac{1}{N} \sum_{n=0}^{N-1} a_n e^{-j2\pi(x'_n + \frac{N-1}{2})(\ell - k)} = \\ &= \frac{1}{N} \sum_{n=0}^{N-1} a_n e^{-j2\pi(x'_n + \frac{N-1}{2})\ell} \cdot e^{j2\pi(-\frac{N-1}{2} + n + \frac{N-1}{2})k} = \\ &= \frac{1}{N} \sum_{n=0}^{N-1} a_n e^{-j2\pi(x'_n + \frac{N-1}{2})\ell} e^{j2\pi n k} = \\ &\stackrel{k \in \mathbb{Z}}{=} \frac{1}{N} \sum_{n=0}^{N-1} a_n e^{-j2\pi(x'_n + \frac{N-1}{2})\ell} = L'_N(\ell). \end{aligned} \quad (50)$$

#### APPENDIX C INFINITE SUMMATION OF (12)

In this appendix section, we want to simplify the following summation

$$\begin{aligned} s_N(\ell) &= \sum_{k=-\infty}^{+\infty} e^{-j2\pi \frac{N-1}{2} (\ell - k)} \text{sinc}(N(\ell - k)) = \\ &= e^{-j2\pi \frac{N-1}{2} \ell} \text{sinc}(N\ell) * \sum_{k=-\infty}^{+\infty} \delta(\ell - k), \end{aligned} \quad (51)$$

where  $*$  and  $\delta(\ell)$  are the linear convolution and the Dirac impulse function, respectively. Due to the convolution becoming a multiplication in the Fourier domain and vice versa, if one considers the inverse Fourier transform of (51), one has

$$\begin{aligned} S_N(x) &= \left( \delta \left( x - \frac{(N-1)}{2} \right) * \frac{1}{N} \text{rect} \left( \frac{x}{N} \right) \right) \cdot \\ &\cdot \frac{1}{2} \sum_{n=-\infty}^{+\infty} \delta(x - n) = \\ &= \text{rect} \left( \frac{x}{N} - \frac{N-1}{2N} \right) \cdot \frac{1}{N} \sum_{n=-\infty}^{+\infty} \delta(x - n). \end{aligned} \quad (52)$$

The multiplication with the rectangle function has the effect of limiting the series in (52) into

$$S_N(x) = \frac{1}{N} \sum_{n=0}^{N-1} \delta(x - n). \quad (53)$$

Leveraging with some modifications the same considerations of Appendix B, one can apply the Fourier transform back from (53), obtaining the Dirichlet kernel shape with the linear phase component due to the AAL translation

$$\begin{aligned} s_N(\ell) &= \frac{1}{N} \sum_{n=0}^{N-1} e^{-j2\pi n \ell} = \\ &= e^{-j2\pi \frac{N-1}{2} \ell} \left( e^{j2\pi \frac{N-1}{2} \ell} \frac{1}{N} \sum_{n=0}^{N-1} e^{-j2\pi 2n \ell} \right) = \\ &= e^{-j2\pi \frac{N-1}{2} \ell} D_N(\ell) = D'_N(\ell). \end{aligned} \quad (54)$$

APPENDIX D  
IDFT DERIVATIONS

The response IDFT in (22) can be obtained by

$$\mathbf{I}'_{\mathbf{A},k} = \sum_{u=0}^{NU-1} \mathbf{I}'_u e^{j2\pi \frac{ku}{NU}} = \sum_{n=0}^{N-1} \mathbf{I}'_n e^{j2\pi \frac{kn}{N}}, k = 0, \dots, NU-1, \quad (55)$$

which is the  $p$ -th element of the IDFT with  $N$  elements of  $(\mathbf{I}')$ , with  $p = \text{mod}_N(k)$ . Therefore, (22) is the sequential repetition of the  $N$  elements of IDFT  $(\mathbf{I}')$ , exactly  $U$  times. Regarding the kernel, from the IDFT definition and (54), one has

$$\begin{aligned} \mathbf{d}'_{\mathbf{A},k} &= \sum_{u=0}^{NU-1} D'_N \left( \frac{u}{NU} \right) e^{j2\pi \frac{ku}{NU}} = \\ &= \sum_{u=0}^{NU-1} \sum_{n=0}^{N-1} e^{-j2\pi n \frac{u}{NU}} e^{j2\pi \frac{ku}{NU}} = \\ &= \sum_{u=0}^{NU-1} \sum_{n=0}^{N-1} e^{j2\pi \frac{u(k-n)}{NU}} = \\ &= \begin{cases} 1 & \text{if } 0 \leq k < N \\ 0 & \text{if } N \leq k < NU-1 \end{cases}. \end{aligned} \quad (56)$$

APPENDIX E  
DERIVATION OF CFAR THRESHOLD

Recalling (33), the noise power is  $\sigma^2 = N^{-1}\sigma_n^2$  and distributed as a complex Gaussian variable. Therefore, the probability that a single noise sample exceeds a threshold  $\zeta$  - corresponding to the desired false alarm probability - is given by the complementary cumulative density function (CCDF) of the Rayleigh distribution

$$P_s^{(\text{FA})} = e^{-\frac{\zeta^2}{\sigma^2}}. \quad (57)$$

Solving (57) for  $\zeta$  yields

$$\zeta = \sqrt{-\sigma^2 \ln(P_s^{(\text{FA})})}. \quad (58)$$

Therefore, the false alarm probability for an angular scan of  $2N-1$  samples is

$$P^{(\text{FA})} = 1 - (1 - P_s^{(\text{FA})})^{2N-1}. \quad (59)$$

Solving for  $P_s^{(\text{FA})}$  and substituting into (58), the CFAR threshold for a desired  $P^{(\text{FA})}$  is

$$\zeta = \sqrt{-\sigma^2 \ln(1 - (P^{(\text{FA})} - 1)^{\frac{1}{2N-1}})}. \quad (60)$$

REFERENCES

[1] H. Viswanathan and P. Mogensen, "Communications in the 6G Era," *IEEE Access*, vol. 8, pp. 57 063–57 074, Mar. 2020.  
[2] J. Liu, H. Liu, Y. Chen, Y. Wang, and C. Wang, "Wireless sensing for human activity: A survey," *IEEE Communications Surveys & Tutorials*, vol. 22, no. 3, pp. 1629–1645, Aug. 2019.  
[3] T. Wild, V. Braun, and H. Viswanathan, "Joint design of communication and sensing for beyond 5G and 6G systems," *IEEE Access*, vol. 9, pp. 30 845–30 857, Feb. 2021.

[4] J. Wang *et al.*, "Beam codebook based beamforming protocol for multi-Gbps millimeter-wave WPAN systems," *IEEE Journal on Selected Areas in Communications*, vol. 27, no. 8, pp. 1390–1399, Oct. 2009.  
[5] S. Hur, T. Kim, D. J. Love, J. V. Krogmeier, T. A. Thomas, and A. Ghosh, "Millimeter wave beamforming for wireless backhaul and access in small cell networks," *IEEE Transactions on Communications*, vol. 61, no. 10, pp. 4391–4403, Oct. 2013.  
[6] X. Zhang, A. F. Molisch, and S.-Y. Kung, "Variable-phase-shift-based RF-baseband codesign for MIMO antenna selection," *IEEE Transactions on Signal Processing*, vol. 53, no. 11, pp. 4091–4103, Nov. 2005.  
[7] A. Alkhateeb, O. El Ayach, G. Leus, and R. W. Heath, "Hybrid precoding for millimeter wave cellular systems with partial channel knowledge," *Proc. Information Theory and Applications Workshop (ITA)*, pp. 1–5, Jun. 2013.  
[8] A. Arora, C. G. Tsinos, B. S. M. R. Rao, S. Chatzinotas, and B. Ottersten, "Hybrid transceivers design for large-scale antenna arrays using majorization-minimization algorithms," *IEEE Transactions on Signal Processing*, vol. 68, pp. 701–714, Dec. 2019.  
[9] R. Rajamäki, S. P. Chepuri, and V. Koivunen, "Analog beamforming for active imaging using sparse arrays," *Proc. 53rd Asilomar Conference on Signals, Systems, and Computers*, pp. 1202–1206, Nov. 2019.  
[10] R. Rajamäki, S. P. Chepuri, and V. Koivunen, "Hybrid beamforming for active sensing using sparse arrays," *IEEE Transactions on Signal Processing*, vol. 68, pp. 6402–6417, Oct. 2020.  
[11] S. Roger, C. Botella-Mascarell, D. Lloria, M. Cobos, and G. Fodor, "Low-complexity AoA and AoD Estimation in the Transformed Spatial Domain for Millimeter Wave MIMO Channels," *Proc. IEEE 32nd Annual International Symposium on Personal, Indoor and Mobile Radio Communications (PIMRC)*, pp. 1–6, Oct. 2021.  
[12] S. Roger, M. Cobos, C. Botella-Mascarell, and G. Fodor, "Fast Channel Estimation in the Transformed Spatial Domain for Analog Millimeter Wave Systems," *IEEE Transactions on Wireless Communications*, vol. 20, no. 9, pp. 5926–5941, Apr. 2021.  
[13] J. Zhang, D. Rakhimov, and M. Haardt, "Gridless Channel Estimation for Hybrid mmWave MIMO Systems via Tensor-ESPRIT Algorithms in DFT BeamSpace," *IEEE Journal of Selected Topics in Signal Processing*, vol. 15, no. 3, pp. 816–831, Mar. 2021.  
[14] Z. Lin, T. Lv, W. Ni, J. A. Zhang, J. Zeng, and R. P. Liu, "Joint estimation of multipath angles and delays for millimeter-wave cylindrical arrays with hybrid front-ends," *IEEE Transactions on Wireless Communications*, vol. 20, no. 7, pp. 4631–4645, Mar. 2021.  
[15] M. D. Zoltowski, M. Haardt, and C. P. Mathews, "Closed-form 2-D angle estimation with rectangular arrays in element space or beamspace via unitary ESPRIT," *IEEE Transactions on Signal Processing*, vol. 44, no. 2, pp. 316–328, Feb. 1996.  
[16] R. M. Lewitt, "Reconstruction algorithms: transform methods," *Proceedings of the IEEE*, vol. 71, no. 3, pp. 390–408, Mar. 1983.  
[17] M. Landmann and G. Del Galdo, "Efficient antenna description for MIMO channel modelling and estimation," *Proc. 7th European Conference on Wireless Technology*, pp. 217–220, May 2004.  
[18] Z. Lin, T. Lv, W. Ni, J. A. Zhang, and R. P. Liu, "Nested hybrid cylindrical array design and DoA estimation for massive IoT networks," *IEEE Journal on Selected Areas in Communications*, vol. 39, no. 4, pp. 919–933, Aug. 2020.  
[19] C. E. Shannon, "Communication in the presence of noise," *Proceedings of the IRE*, vol. 37, no. 1, pp. 10–21, Jan. 1949.  
[20] D. Jackson, "On the accuracy of trigonometric interpolation," *Transactions of the American Mathematical Society*, vol. 14, no. 4, pp. 453–461, Oct. 1913.  
[21] V. K. Jain, W. L. Collins, and D. C. Davis, "High-accuracy analog measurements via interpolated FFT," *IEEE Transactions on Instrumentation and Measurement*, vol. 28, no. 2, pp. 113–122, Jun. 1979.  
[22] R. Schmidt, "Multiple emitter location and signal parameter estimation," *IEEE transactions on antennas and propagation*, vol. 34, no. 3, pp. 276–280, Mar. 1986.  
[23] V. M. Baronkin, Y. V. Zakharov, and T. C. Tozer, "Cramer-Rao lower bound for frequency estimation in multipath Rayleigh fading channels," *Proc. IEEE International Conference on Acoustics, Speech, and Signal Processing. Proceedings (Cat. No. 01CH37221)*, pp. 2557–2560, Aug. 2001.  
[24] B. D. Steinberg, *Principles of aperture and array system design: Including random and adaptive arrays*. New York, NY, USA: John Wiley & Sons, 1976.  
[25] M. A. Pinsky, *Introduction to Fourier analysis and wavelets*. Providence, RI, USA: American Mathematical Soc., 2008.  
[26] R. Priemer, *Introductory signal processing*. Singapore: World Scientific, 1990.

- [27] R. T. Hocht and S. A. Kassam, "The unifying role of the coarray in aperture synthesis for coherent and incoherent imaging," *Proceedings of the IEEE*, vol. 78, no. 4, pp. 735–752, Apr. 1990.
- [28] H. L. Van Trees, *Optimum array processing: Part IV of detection, estimation, and modulation theory*. Hoboken, NJ, USA: John Wiley & Sons, 2004.
- [29] D. G. Zill, *Advanced engineering mathematics*. Burlington, MA, USA: Jones & Bartlett Publishers, 2020.
- [30] U. Spagnolini, *Statistical Signal Processing in Engineering*. Hoboken, NJ, USA: John Wiley & Sons, 2018.
- [31] M. Henninger, S. Mandelli, M. Arnold, and S. ten Brink, "A computationally efficient 2D MUSIC approach for 5G and 6G sensing networks," *Proc. IEEE Wireless Communications and Networking Conference (WCNC)*, pp. 210–215, Apr. 2022.
- [32] J. Rissanen, "Modeling by shortest data description," *Automatica*, vol. 14, no. 5, pp. 465–471, Sep. 1978.
- [33] K. Toraichi, K. Katagishi, I. Sekita, and R. Mori, "Computational complexity of spline interpolation," *International Journal of Systems Science*, vol. 18, no. 5, pp. 945–954, May 1987.
- [34] "TS 38.211. NR; Physical channels and modulation," Standard Technical Specification TS 38.211 V17.0.0, 3GPP, 2022.
- [35] M. A. Richards and J. A. Scheer, *Principles of Modern Radar: Radar Applications*. Raleigh, NC, USA: SciTech Pub., 2014.
- [36] D. H. Johnson and D. E. Dudgeon, *Array signal processing: concepts and techniques*. New York, NY, USA: Simon & Schuster, Inc., 1992.